Supplementary Information

Organic Melt, Electride and CVD Induced In-situ Deposition of Luminescent Lanthanide Imidazolate MOFs on Nanostructured Alumina

Larissa Valerie Meyer, Joachim Vogt, Helmut Schäfer, Martin Steinhart, Rolf Böttcher , Andreas Pöppl, Marit Mai, Claus Feldmann and Klaus Müller-Buschbaum

Experimental Details

In-situ coating of $^{3}_{\infty}[Sr_{0.95}Eu_{0.05}(Im)_2]$ via electride approach and melt approach with different annealing times (1, 12 and 48 hours)

Electride approach:

Strontium/europium metal (1*10-3 mol; STREM 99.5 % / Sigma Aldrich 99.95%; ratio: Sr/Eu: x = 0.05: m(Sr) = 83.2 mg, m(Eu) = 7.6 mg), 1*H*-imidazole (3 mmol, 204 mg, Acros Organics, 99%) and an AAO membrane of suitable size were sealed in an evacuated DURAN^{TM} glass ampoule ($6*10^{-3}$ mbar). 5 ml of ammonia (Linde, 99.999%) were condensed with liquid nitrogen into the ampoule. Subsequently cooling of the reaction mixture was reduced from -78 °C to -55 °C in 5 minutes, after that room temperature was achieved with a thawing rate of 20K/h. The color of the reaction mixture immediately changed into dark blue on the metal pieces surface. The dark blue color changed to yellow at contact with 1*H*-imidazole in liquid ammonia. Evaporation of ammonia results in the formation of vibrant yellow microcrystalline product. The ampoule was sealed under vacuum ($3*10^{-2}$ mbar) and annealing was carried out in a tube oven by heating up to 220 °C within 10 minutes. Temperature was kept constant for 36 h and then cooled to room temperature within 2 h. Excess 1*H*-imidazole was removed *via* sublimation. The remaining product was a fine vibrant yellow powder as well as a coated alumina substrate.
Micro analysis (bulk): $^{3}_{\infty}[Sr_{0.95}Eu_{0.05}(Im)_2]$: C 32.01%, H 2.78%, N 24.72%; calc.: C 32.03%, H 2.69%, N 24.9%.
MIR (ATR) (bulk): $^{3}_{\infty}[Sr_{0.95}Eu_{0.05}(Im)_2]$: (3310 s, 3123 w, 1529 w, 1483 w, 1452 m, 1423 w, 1328 w, 1220 m, 925 m, 914 w, 828 m, 768 m, 755 m) cm^{-1}.

Melt approach with different annealing times (1, 12 and 48 hours)

Weigth-in analogue to the above described. All starting materials were sealed in an evacuated DURAN™ glass ampoule ($1*10^{-3}$ mbar) and then annealing was carried out in a tube oven by heating up to 215 °C within a heating rate of 50 K/h. Temperature was kept constant for one, 12 and 48 hours, respectively. After that, the reaction mixture was cooled to room temperature with a rate of 50 K/h. Excess 1*H*-imidazole was removed *via* sublimation. The remaining product was a fine yellow powder as well as a coated alumina substrate.

12 hours annealing time:
Micro analysis (bulk): $^{3}_{\infty}[Sr_{0.95}Eu_{0.05}(Im)_2]$: C 31.46%, H 2.61%, N 24.68%; calc.: C 32.03%, H 2.69%, N 24.9%.
MIR (ATR) (bulk): $^{3}_{\infty}[Sr_{0.95}Eu_{0.05}(Im)_2]$: (3592 w, 3310 m, 3124 m 3014 m, 2914 m, 2825 m, 2700 m, 2614 m, 1482 w, 1451 m, 1425 m, 1325 m, 1221 w, 1075 m, 1065 s, 926 m, 914 m, 827 m, 754 s) cm^{-1}.

48 hours annealing time:
Micro analysis (bulk): $^{3}_{\infty}[Sr_{0.95}Eu_{0.05}(Im)_2]$: C 31.86 %, H 3.02 %, N 23.92 %; calc.: C 32.03%, H 2.69%, N 24.9%.
MIR (ATR) (bulk): $^{3}_{\infty}[Sr_{0.95}Eu_{0.05}(Im)_2]$: (3123 m, 2908 m, 2770 s, 2697 s, 2613 m, 1683 m, 1671 m, 1448 m, 1054 s, 923 m, 828 m, 753 s) cm^{-1}.

In-situ coating and *CVD* deposition of $^{3}_{\infty}[Tb(Im)_3]$ and $^{3}_{\infty}[Ce(Im)_3ImH]\cdot ImH$ *via* melt approach

Cerium/ terbium metal (1*10-3 mol; STREM 99.5 % m(Ce) = 140 mg / m(Tb) = 159 mg), 1*H*-imidazole (6 mmol (Ce), 408 mg; 4 mmol (Tb), 272 mg, Acros Organics, 99%) and an AAO membrane of suitable size were filled in a DURAN^{TM} glass ampoule. Additionally, a catalytically amount of Hg (0.5 mmol, 100 mg, Riedel de Häen, 99%) was used in the synthesis of $^{3}_{\infty}[Tb(Im)_3]$. The ampoule was sealed under vacuum ($1*10^{-3}$ mbar) and annealing was carried out in a tube oven by heating up to 180 °C within 6 hours. Temperature was kept constant for 168 h and then cooled to room temperature within 6 h. Excess 1*H*-imidazole was removed *via* sublimation. In each case the remaining product was a fine colourless powder as well as a coated alumina substrate.

Micro analysis (bulk): $^{3}_{\infty}[Tb(Im)_3]$: C 30.45 %, H 2.95 %, N 23.71 %; calc.: C 30.02%, H 2.52%, N 23.36%.
MIR (ATR) (bulk): $^{3}_{\infty}[Tb(Im)_3]$: (3125 w, 3107 w, 3015 w 2911 w, 2818 w, 2703 w, 2610 w, 1592 w, 1543 w, 1437 w, 1388 m, 1374 w, 1327 w, 1253 w, 1229 m, 1136 w, 1107 w, 1070 s, 963 w, 938 s, 855 w, 751 m) cm^{-1}.
Micro analysis (bulk): $^{3}_{\infty}[Ce(Im)_3ImH]\cdot ImH$: C 36.93 %, H 3.58 %, N 28.17 %; calc.: C 37.73%, H 3.59%, N 29.33%.
MIR (ATR) (bulk): $^{3}_{\infty}[Ce(Im)_3ImH]\cdot ImH$: (3124 m, 3100 m, 3017 m, 2909 m, 2819 m, 2790 m, 2614 s, 2540 m, 1545 w, 1460 w, 1450 m, 1326 w, 1263 w, 1230 w, 1147 w, 933 s, 896 w, 841 m, 828 m, 755 m, 739 m) cm^{-1}.

In order to prove the *CVD* deposition a separately ampoule was chosen. The experimental setup is shown in figure S1. Due to the setup there is no direct contact between the melt and the AAO substrate. All starting materials were put together as well as the AAO membranes were placed in the tapering of the ampoule. After that the ampoule was sealed under vacuum ($1*10^{-3}$ mbar) and annealing was carried out in a tube oven by heating up to 180 °C within 6 hours. Temperature was kept constant for 168 h and then cooled to room temperature within 6 h. Both the resulting bulk material and the AAO membrane were transferred into a second ampoule and excess 1*H*-imidazole was removed *via* sublimation.
Micro analysis and MIR investigations of the corresponding bulk materials are in accordance with the data above.

Sorption measurements

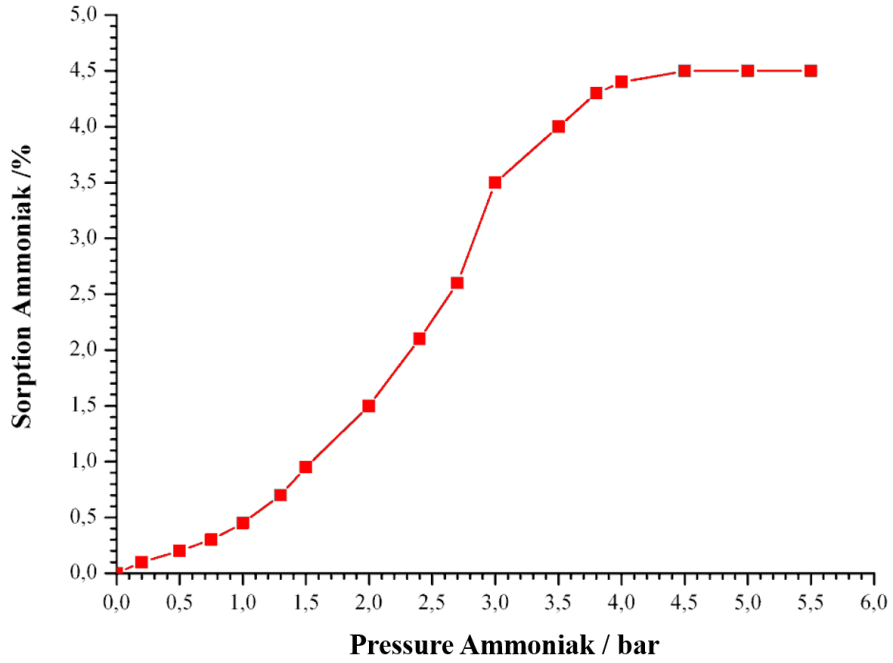

Figure S1: Sorption of NH_3 (-78°C) on $^{3}_{\infty}[Tb(Im)_3]$ reaches its maximum 4.5 bar pressure. The uptake is mainly observed above atmosphere pressure and ranges up to 92 cm^3/g = 4.5 mass-%.

X-ray Powder Diffraction

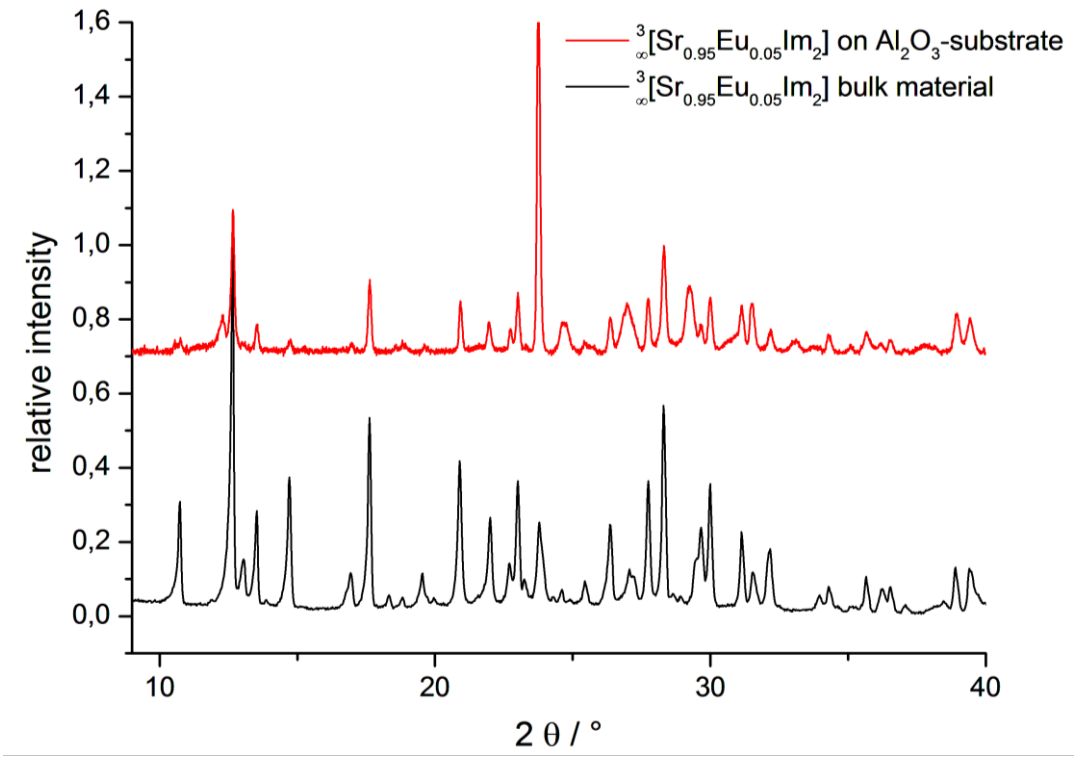

Fig. S2: Powder diffractogram of $^3_\infty$[$Sr_{0.95}Eu_{0.05}(Im)_2$] coated AAO substrate in comparison to the powder diffractogram of the corresponding bulk material.

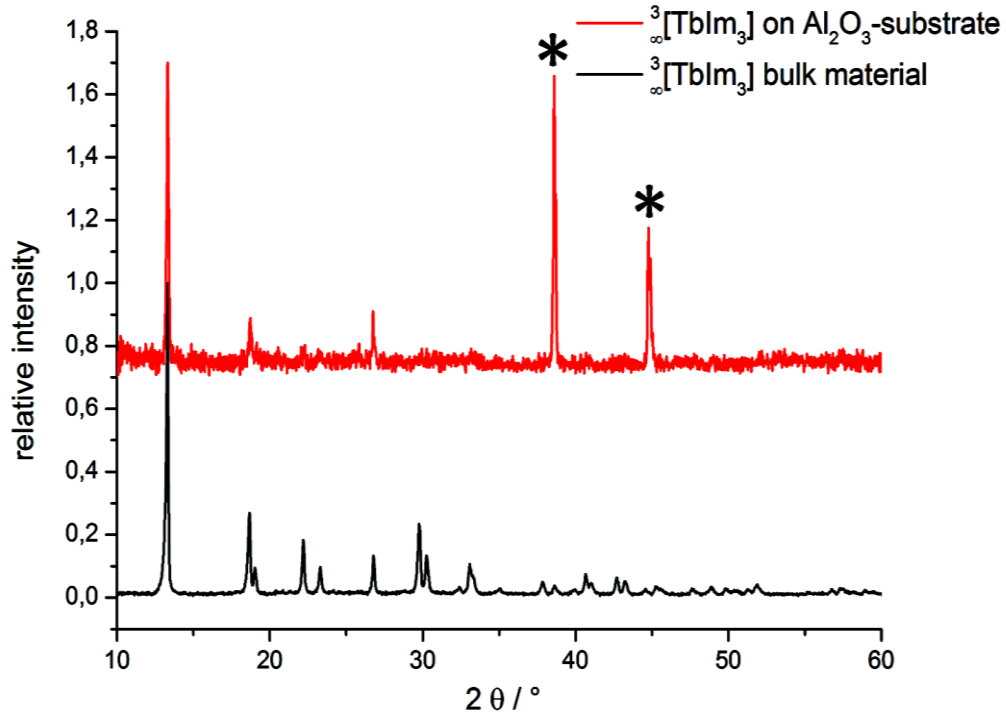

Fig. S3: Powder diffractogram of $^3_\infty$[$Tb(Im)_3$] coated AAO substrate with an Al-edge in comparison to the powder diffractogram of the corresponding bulk material; the black stars assign aluminium (PDF 00-001-1180), attributed to the aluminium edge of the AAO substrates.

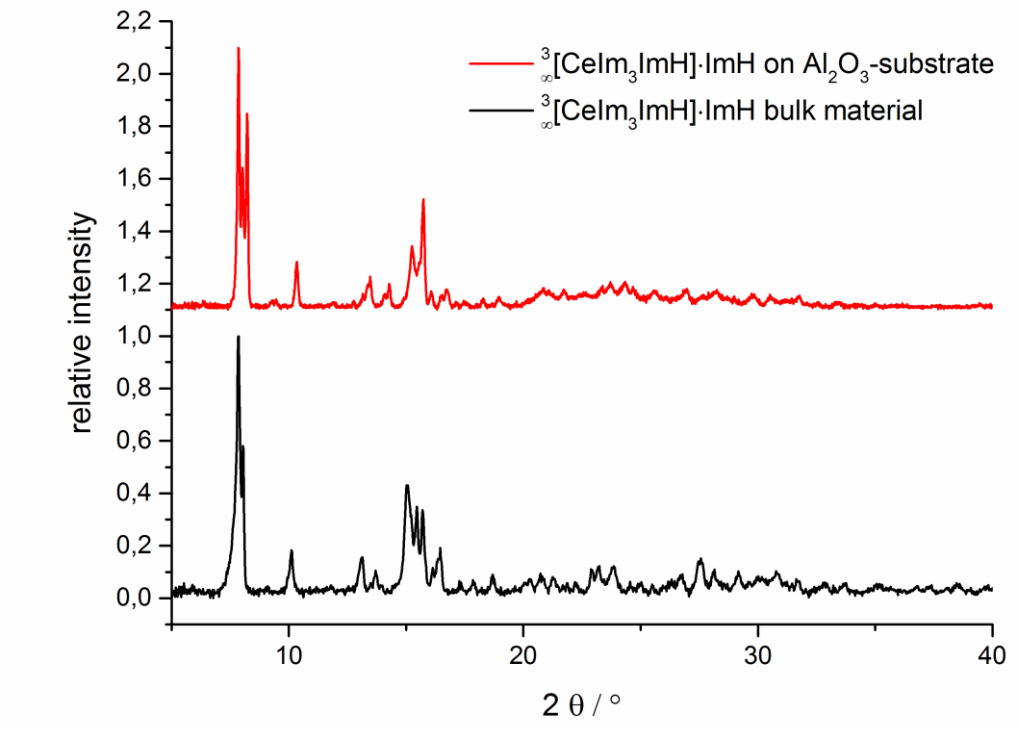

Fig. S4: Powder diffractogram of $^3_\infty$[Ce(Im)$_3$ImH]·ImH scraped off a coated AAO substrate in comparison to the powder diffractogram of the corresponding bulk material.

Photoluminescence spectroscopy

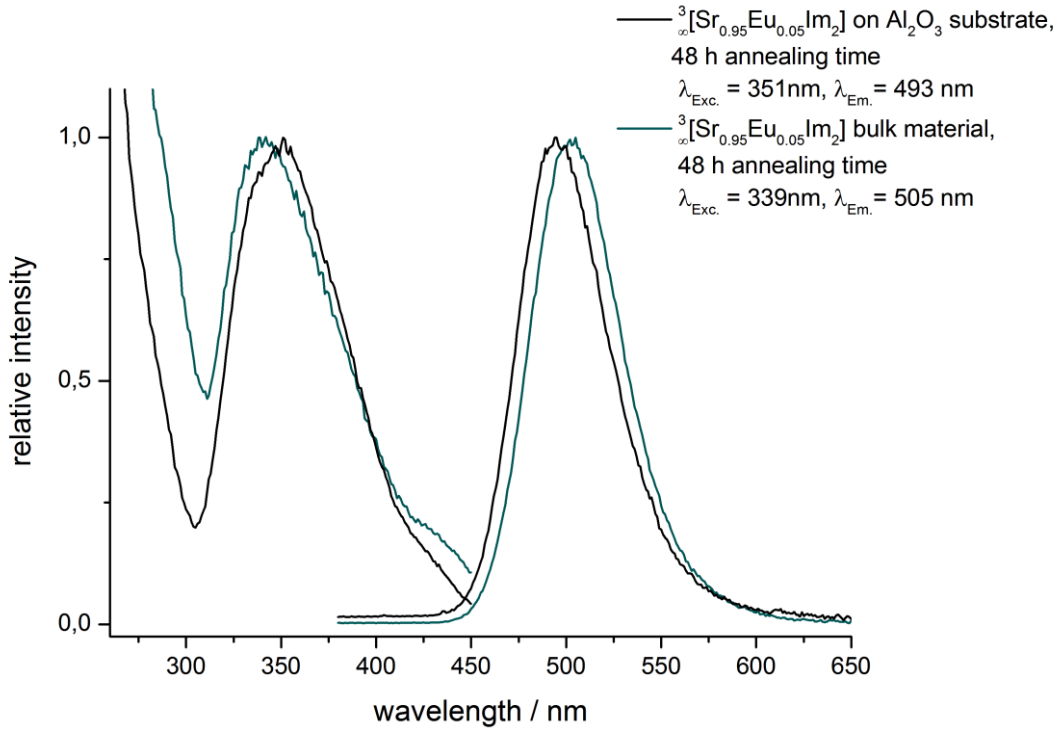

Fig. S5: Excitation and emission spectra of $^3_\infty$[Sr$_{0.95}$Eu$_{0.05}$(Im)$_2$] coated AAO membranes and the bulk material after an annealing time of 48 hours.

Electron Microscopy and EDX / element mapping

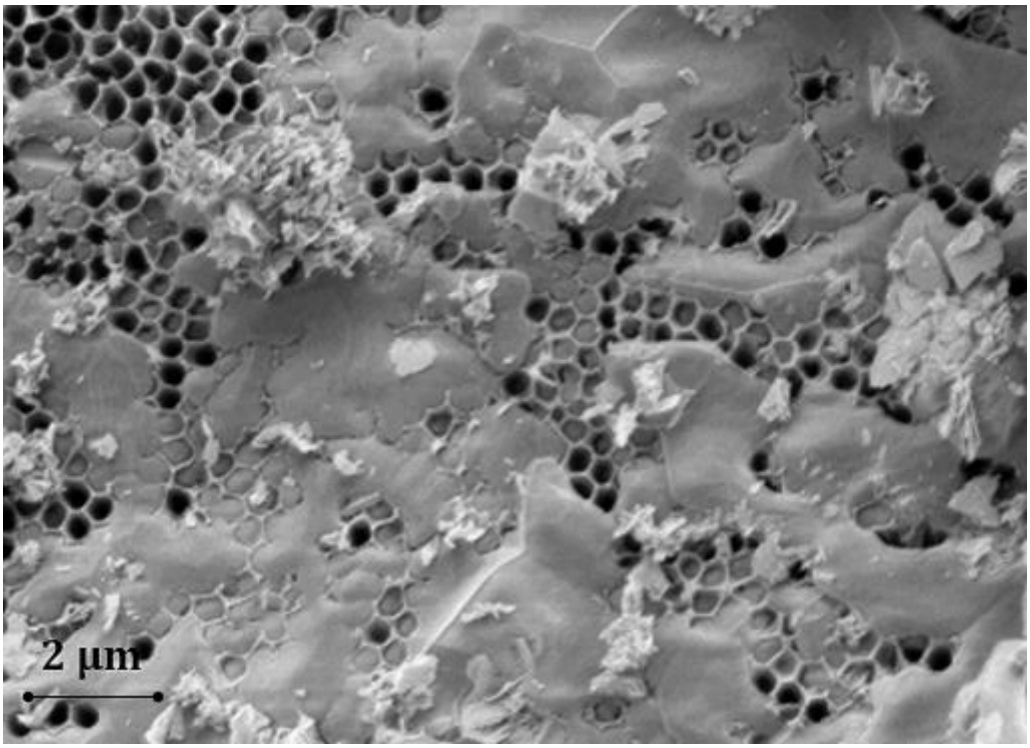

Fig. S6: Scanning electron microscopy (SEM) images of AAO (pore diameter 400 nm; pore depth 100 µm) coated with $^{3}_{\infty}[Sr_{0.95}Eu_{0.05}(Im)_2]$ from electride approach.

EDX point-ID measurements

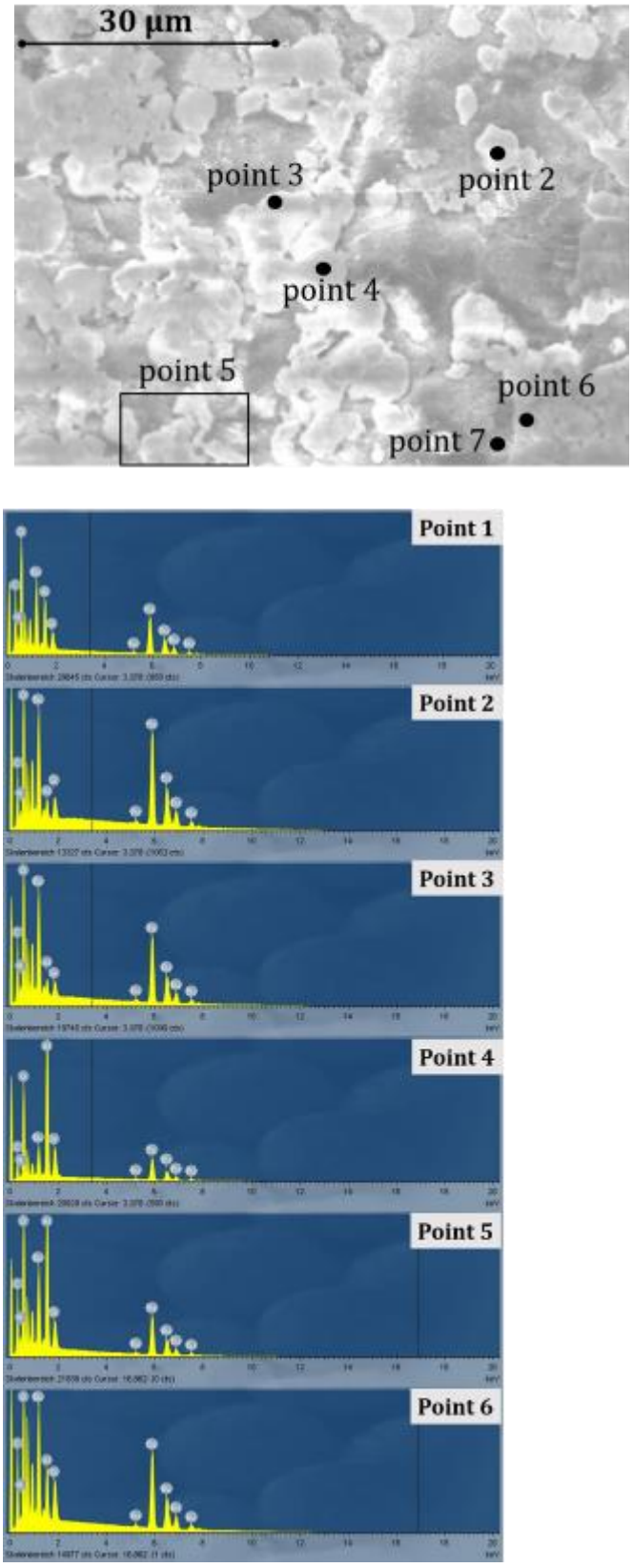

Fig. S7: SEM and EDX point ID (top) and the corresponding analyzerspectra (bottom) of the barite rose analogue crystals achieved from the electride approach of the in-situ coating method for films of $^{3}{}_{\infty}[Sr_{0.95}Eu_{0.05}(Im)_2]$ by liquid ammonia.

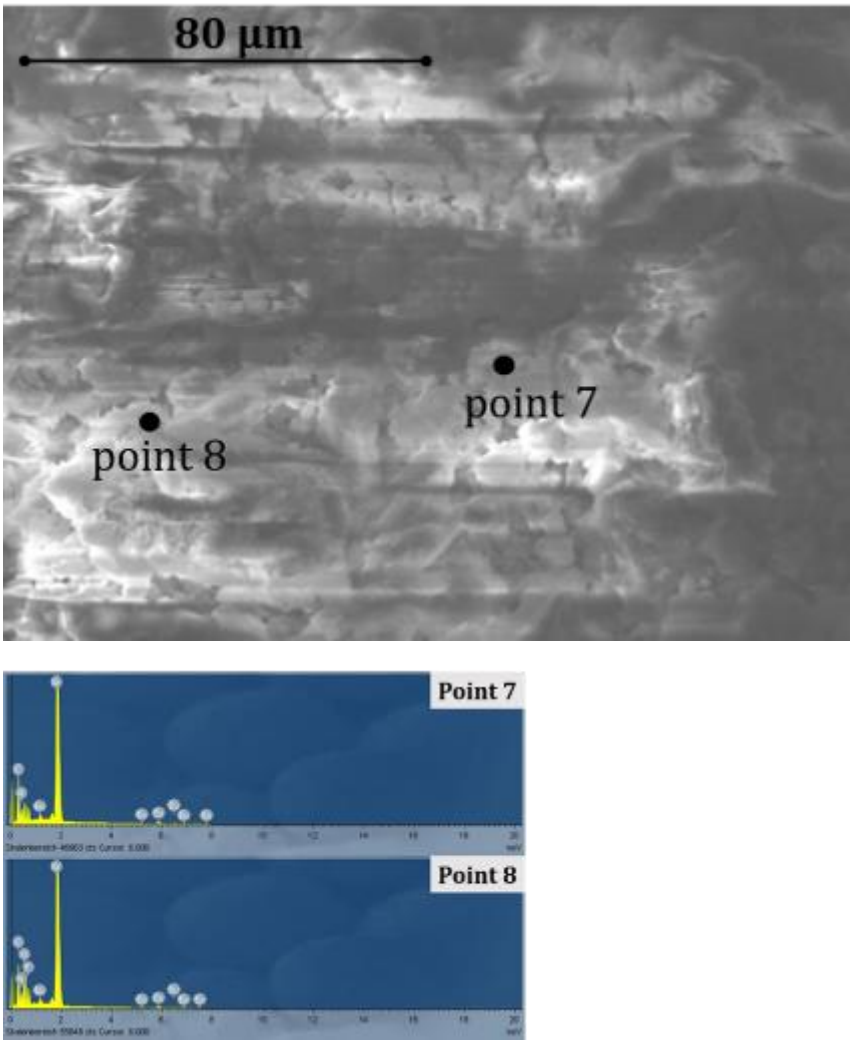

Fig. S8: SEM and EDX point ID (top) and the corresponding analyzerspectra (bottom) of the bulk material $^{3}_{\infty}[Sr_{0.95}Eu_{0.05}(Im)_2]$ achieved from the electride approach by liquid ammonia.

Table 1: Atomic percentages of the ratio strontium/europium achieved by EDX point-ID measurements

EDX point ID measurements of the barite rose analogue crystals out of the electride approach	
Analyzer point	Ratio strontium/europium in atomic percentages
Point 1	17.41/82.59
Point 2	10.12/89.88
Point 3	9.84/90.16
Point 4	35.77/64.23
Point 5	23.56/76.44
Point 6	18.85/81.15
EDX point ID measurements of the bulk material $^{3}_{\infty}[Sr_{0.95}Eu_{0.05}Im_2]$	
Analyzer point	Ratio strontium/europium in atomic percentages
Point 7	96.21 / 3.79
Point 8	97.03/2.97

Electron Microscopy and EDX / element mapping

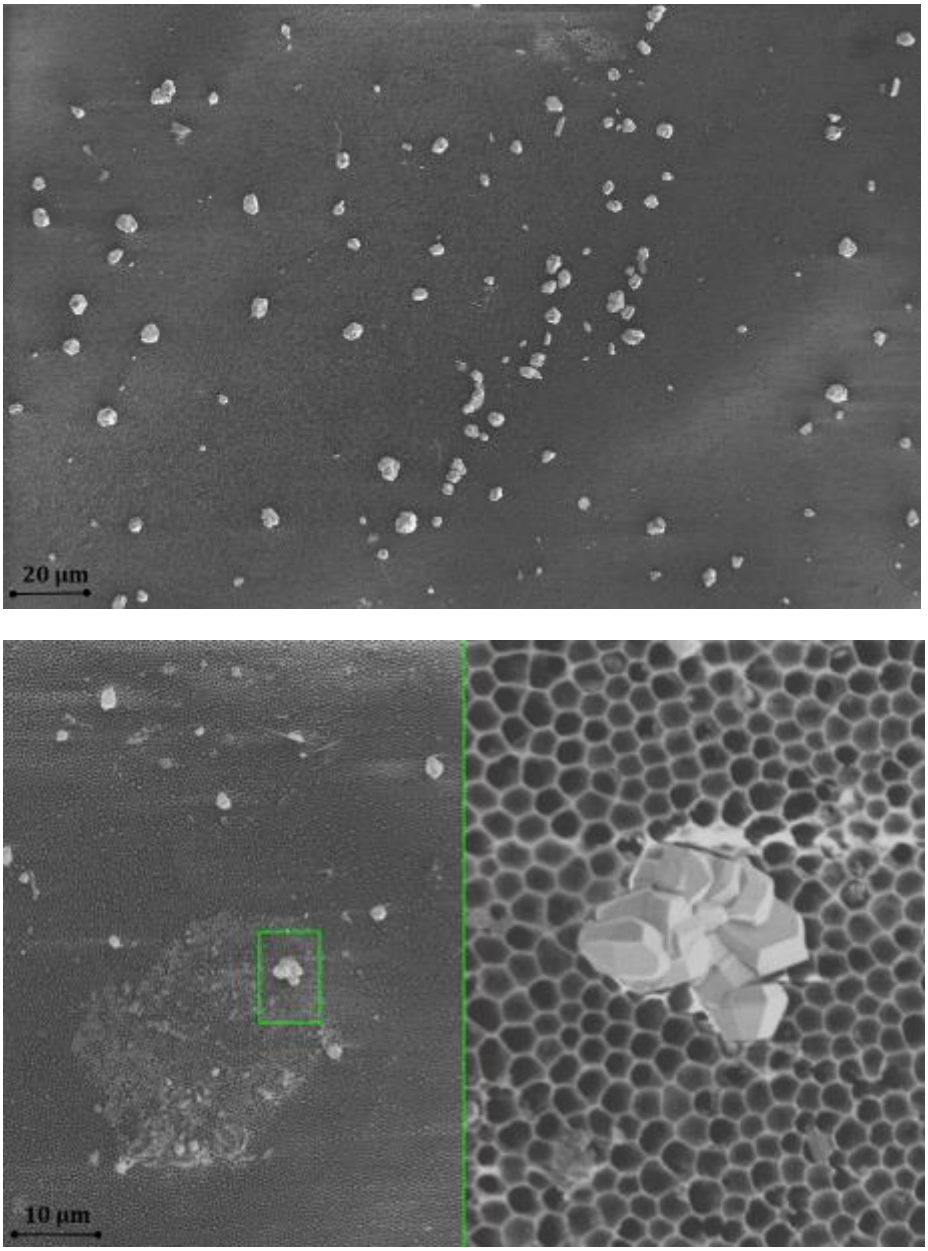

Fig. S9: Scanning electron microscopy (SEM) images of the CVD deposition of $^{3}_{\infty}$[Ce(Im)$_3$ImH]·ImH on AAO substrate (pore diameter 400 nm; pore depth 100 µm) (top and bottom); the deposition occurred without any contact to the melt synthesis; experimental setup given in Fig. S1.

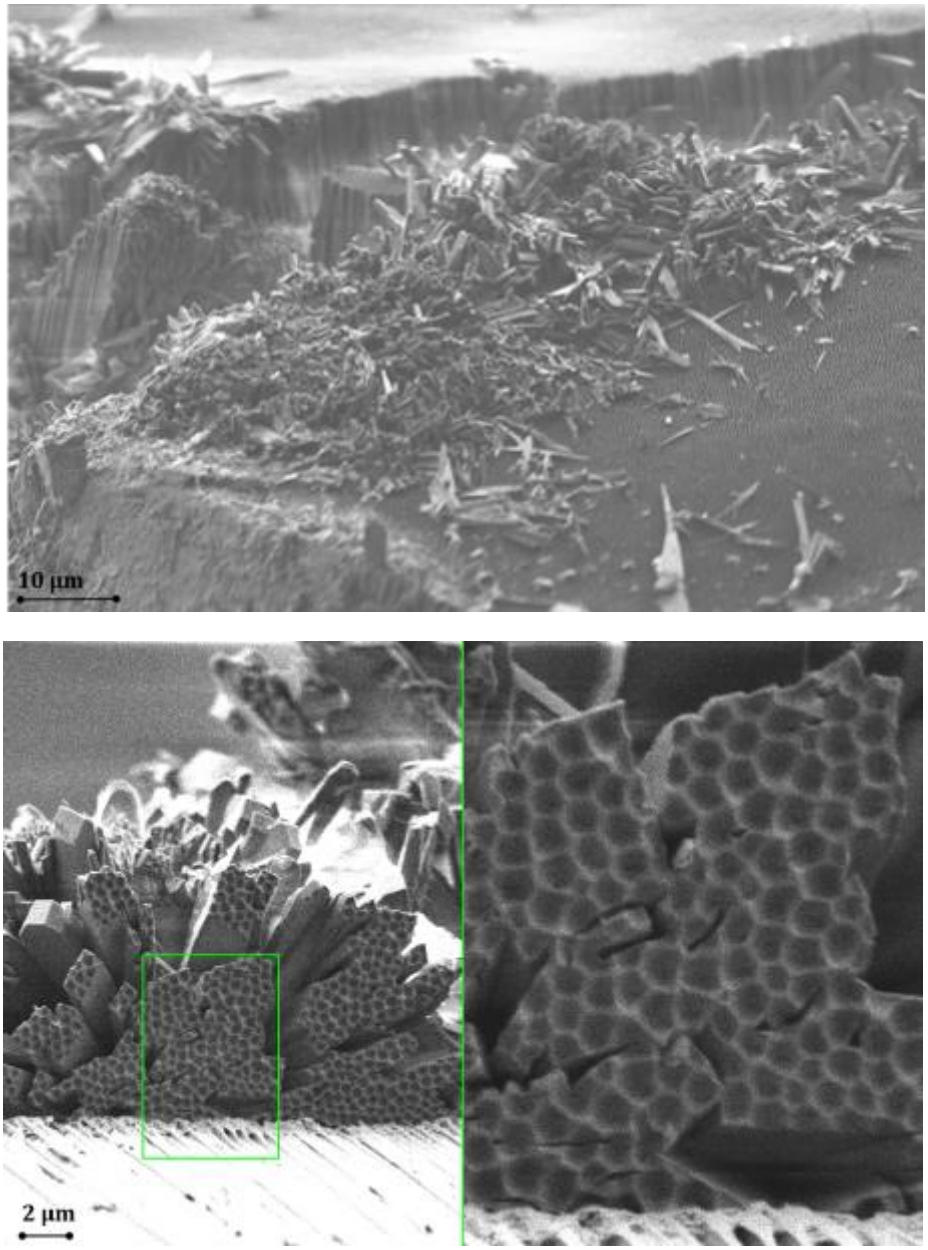

Fig. S10: Scanning electron microscopy (SEM) images of the CVD deposition of $^{3}_{\infty}[Tb(Im)_3]$ on AAO substrate (pore diameter 400 nm; pore depth 100 µm) (top and bottom); the deposition occurred without any contact to the melt synthesis; experimental setup given in Fig. S1.

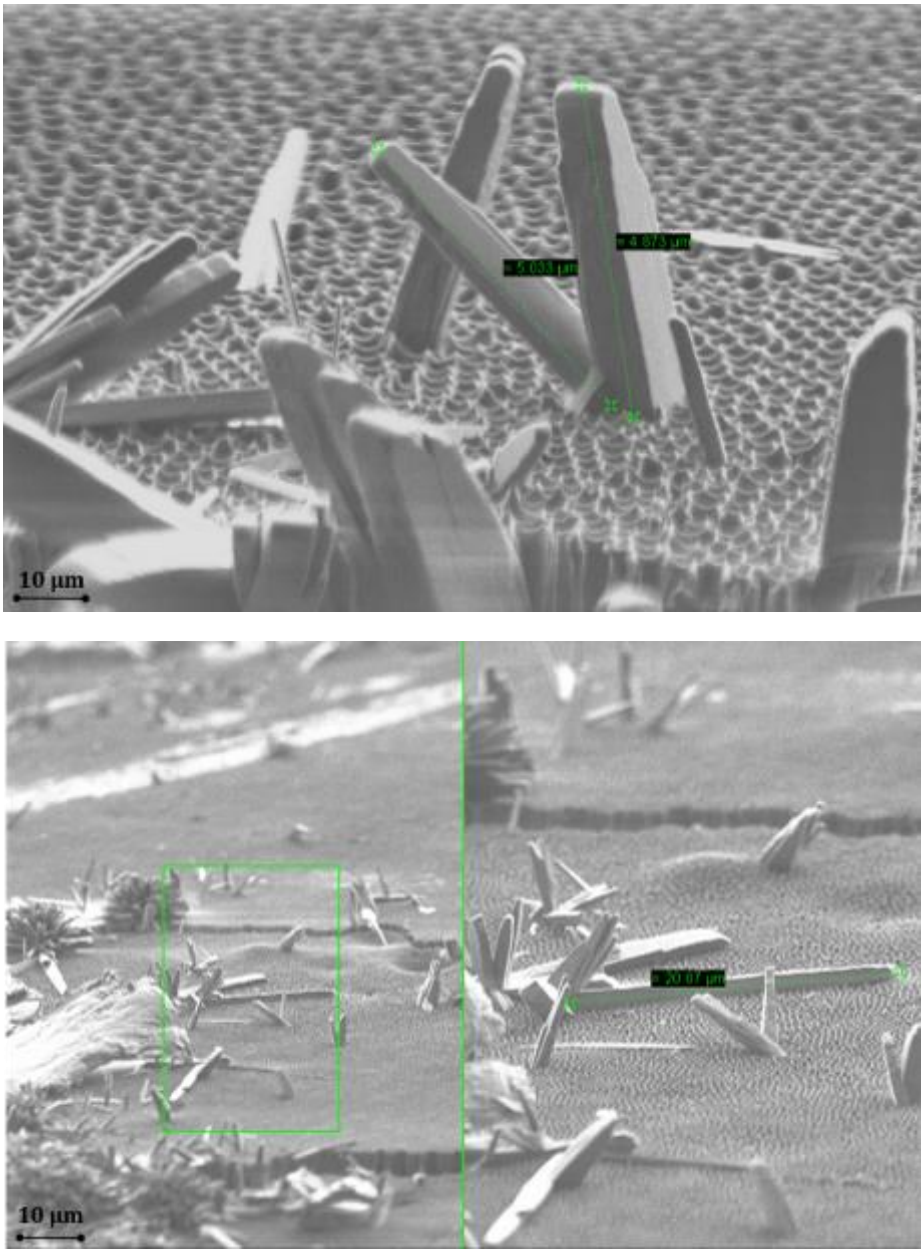

Fig. S11: Scanning electron microscopy (SEM) images of the CVD deposition of $^{3}_{\infty}[Tb(Im)_3]$ on AAO substrate (pore diameter 400 nm; pore depth 100 µm) (top and bottom); the deposition occurred without any contact to the melt synthesis; experimental setup given in Fig. S1.

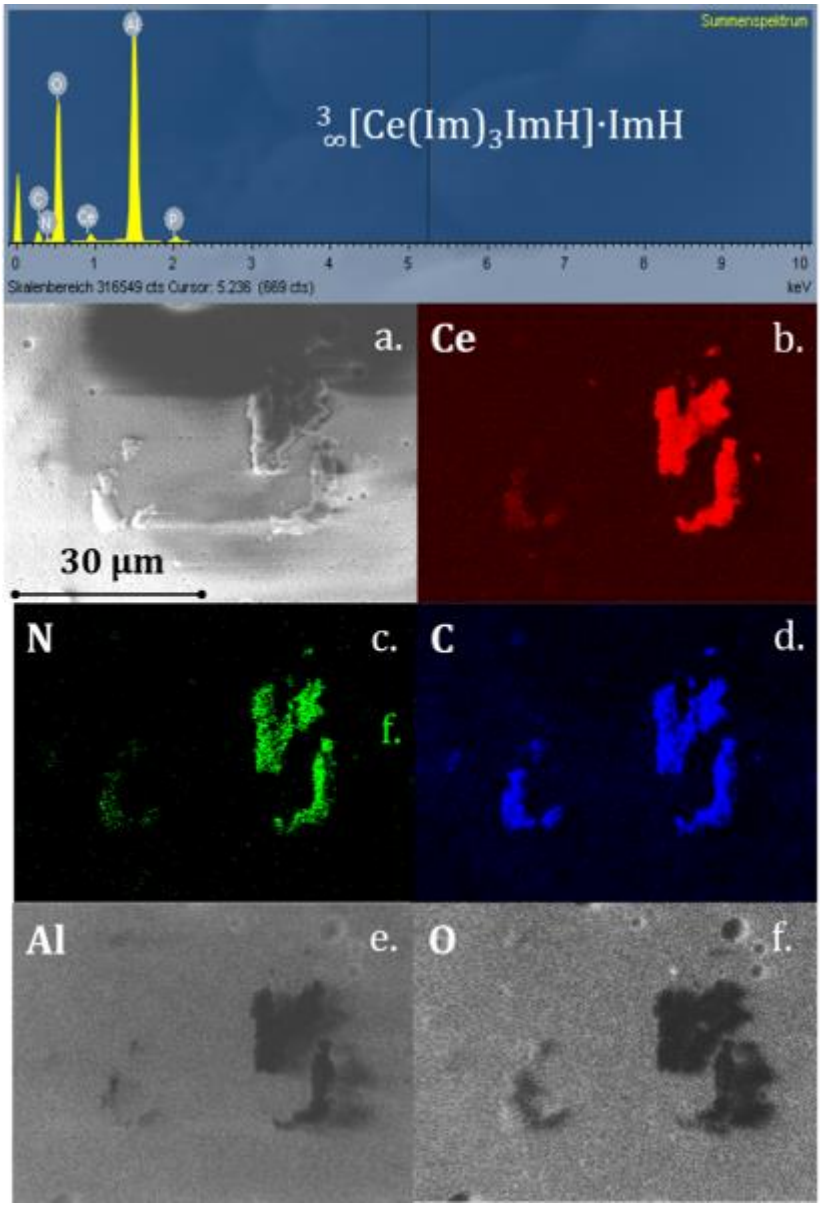

Fig. S12: EDX spectrum of the visualized excerpt (top), a. SEM image of CVD-like deposited crystals of $^{3}_{\infty}$[Ce(Im)$_3$ImH]·ImH on AAO substrate; b – f referring EDX element mapping for Ce, N, C, Al and O.

EPR spectroscopy

In a solid the divalent Eu^{II} ion ($4f^7$, $L = 0$) with a total electron spin $S = 7/2$ is subjected to crystal fields due to the electric charges and dipole moments of the lattice constituents in the neighbourhood of the europium ions. The crystal fields lead via spin-orbit coupling to the so-called zero field splitting (zfs) or fine structure (fs) splitting of the spin states.[1] In the EPR spectrum of an $S = 7/2$ spin system we expect eight allowed spin transitions according to the selection rule $\Delta M_S = \pm 1$ where M_S refers to the magnetic spin quantum number. Furthermore additional transitions from forbidden transitions according to selection rules $\Delta M_S = \pm 2, \pm 3$ may be observed. The corresponding magnetic field positions of these fs transitions depend strongly on the orientation of the external magnetic field with respect to the symmetry axes of the crystal field. Besides the zfs an additional hyperfine (hf) splitting is expected due to the magnetic interaction between the electron spin and the nuclear spins of the two europium isotopes ^{151}Eu (nuclear spin $I = 5/2$, natural abundance 49.1 %) and ^{152}Eu (nuclear spin $I = 5/2$, natural abundance 51.1 %). The EPR spectra of Eu^{II} ions can be described by the spin Hamiltonian operator[1]

$$\hat{H} = \mu_B g \vec{S}\vec{B} + \hat{H}_{zfs} + \vec{S}A\vec{I} \qquad (1)$$

where the first term is the electron Zeeman interaction with the g value and the Bohr's magneton μ_B and the last term is the hf interaction with the hf interaction constant A. The operator $\hat{H}_{zfs}$ describes the zfs and depends on local symmetry at the Eu^{II} site.
In case of cubic symmetry

$$\vec{H}_{zfs}^{cub} = B_4^0\left(\hat{O}_4^0 + 5\hat{O}_4^4\right) + B_6^0\left(\hat{O}_6^0 + 21\hat{O}_6^6\right) \qquad (2)$$

with the Stevens operators $\hat{O}_k^q$ (q = 0, 4, 6 and k = 4, 6) and zfs parameters B_4^0 and B_6^0. For tetragonal symmetries $\hat{H}_{zfs}$ becomes

$$\vec{H}_{zfs}^{tetr} = B_2^0\hat{O}_2^0 + B_4^0\hat{O}_4^0 + B_4^4\hat{O}_4^4 + B_6^0\hat{O}_6^0 + B_6^4\hat{O}_6^4 + B_6^6\hat{O}_6^6\,. \qquad (3)$$

If the Eu^{II} site has a local orthorhombic symmetry two more terms must be included in the zfs operator

$$\vec{H}_{zfs}^{tetr} = B_2^0\hat{O}_2^0 + B_4^0\hat{O}_4^0 + B_4^4\hat{O}_4^4 + B_6^0\hat{O}_6^0 + B_6^4\hat{O}_6^4 + B_6^6\hat{O}_6^6 + B_2^2\hat{O}_2^2 + B_4^2\hat{O}_4^2\,. \qquad (4)$$

The EPR spectrum of a powder sample is the weighted average of all orientation dependent single crystal spectra of system and consists of relatively broad peaks that can be assigned to specific orientations of the external magnetic field with respect to the symmetry axes of the local crystal field at the paramagnetic ion.[1] from the position of these peaks in the powder spectrum the spin Hamiltonian parameters g, A, and B_k^q with q = 0, 2, 4, 6 and k = 2, 4, 6.
The spin Hamiltonian parameters of the samples $^3{}_\infty[Sr_{1-x}Eu_x(Im)_2]$ with x = 0.01, 0.05 and $^3{}_\infty[Sr_{0.95}Eu_{0.05}(Im)_2(ImH)_2]$ have been determined from the corresponding EPR powder spectra by a numerical fitting procedure of the spin Hamiltonian in eq. (1) with the zfs Hamiltonian in eq. (4) using MATLAB© and the Easyspin toolbox.[2] The zfs parameters and B_k^q with q = 0, 4, 6 and k = 6 are known to be small for Eu^{II} from a series of single crystal studies and lead just to displacements of the peaks in the powder patterns that are smaller than their line widths.[1] Therefore these parameters have been neglected in our fitting procedure. Table 1 summarizes the spin Hamiltonian parameters of the three identified Eu^{II} species. In all cases isotropic hfi constants of $|A_{iso}| = 97$ MHz for ^{151}Eu and $|A_{iso}| = 143$ MHz for ^{152}Eu have been found. The zfs parameters of both species A and B exhibit a small, continuous temperature dependence (Tab.2 and 3) which might be related to thermal expansion or contraction effects of the $^3{}_\infty[Sr_{1-x}Eu_x(Im)_2]$ lattice.

The sample $^3{}_\infty[Sr_{1-x}Eu_x(Im)_2]$, x = 1, shows a single almost isotropic signal of Lorentzian line shape with a g value of $g = 1.9924 \pm 0.0010$ and a line width at Q-band of $\Delta B_{pp} = 774$ G. Illumination of the sample with the full spectrum of high pressure mercury arc lamp (HBO 100) at $T = 8$ K did not influence the intensity of the Eu^{II} EPR signal. Such isotropic EPR signals are typical for magnetically undiluted materials and are caused by $\Delta M_S = \pm 1$ transitions.[1] Forbidden $\Delta M_S = \pm 2$ transitions can be observed at half field and are indicative for spin systems with large dipole-dipole interactions[3] which prevent the observation of zfs and hfi for such systems. Therefore we may assign the signal to Eu^{II} ions in high local concentrations as expected for the pure europium

material $^3_\infty$[Eu(Im)$_2$]. Assuming four formula units per unit cell[4] and a unit cell volume V = 705 · 10^6 pm^3 provides a Eu^{II} concentration n = 5.67 · 10^{27} m^{-3}. Then the peak-to-peak line width ΔB_{pp}^G = 1885 G of an isotropic Eu^{II} EPR signal, broadened by dipole-dipole interactions, can be calculated according to

$$\Delta B_{pp}^G = 2\sqrt{\left\langle \Delta B^2 \right\rangle_G} \tag{5}$$

where

$$\left\langle \Delta B^2 \right\rangle_G = 5.1\left(\frac{g\mu_0\mu_\beta n}{4\pi}\right)^2 S(S+1) \tag{6}$$

is the second moment of the $\Delta M_S = \pm 1$ signal with Gaussian line shape.[3,5] As ΔB_{pp}^G = 1885 G is substantially larger than the experimentally obtained line width ΔB_{pp} = 774 G we must assume the Eu^{II} EPR signal in $^3_\infty$[Eu(Im)$_2$] is narrowed by magnetic exchange interaction among the Eu^{II} ions. If we introduce an exchange field[6]

$$B_e = \frac{J_e}{g\mu_\beta}\sqrt{2.83\,S(S+1)} \tag{7}$$

with an exchange coupling parameter J_e the line width of the Lorentzian part of the exchange narrowed signal can be computed by

$$\Delta B_{pp}^L = \frac{2}{\sqrt{3}}\frac{\left\langle \Delta B^2 \right\rangle_G}{B_e} \cdot \tag{8}$$

Using eq. 7 and 8 and assuming $\Delta B_{pp} \approx \Delta B_{pp}^L$ we can estimate for the exchange interaction between the Eu^{II} ions an exchange coupling parameter J_e = 0.0185 cm^{-1} from the experimental line width ΔB_{pp} and the computed second moment $\langle \Delta B^G \rangle_G$

$$J_e = \frac{2}{\sqrt{3}}\frac{\left\langle \Delta B^2 \right\rangle_G}{\frac{\Delta B_{pp,\,fit}^L}{g\mu_\beta}\sqrt{2.83\,S(S+1)}} \tag{9}$$

Fig. S12 shows a comparison of the room temperature Eu^{II} X-band EPR spectra of $^3_\infty$[Sr$_{1-x}$Eu$_x$(Im)$_2$] with x = 0.01, 0.05, x = 1. Detailed spectra of the samples of $^3_\infty$[Sr$_{1-x}$Eu$_x$(Im)$_2$] with x = 0.01, 0.05, x = 1 and in $^3_\infty$[Sr$_{0.95}$Eu$_{0.05}$(Im)$_2$(ImH)$_2$] are presented in Fig. S13 – S21.

Tab. 2: Spin Hamiltonian parameters of the Eu^{II} species A, B, and C found for $^{3}_{\infty}[Sr_{1-x}Eu_x(Im)_2]$ with x = 0.01, 0.05 and $^{3}_{\infty}[Sr_{0.95}Eu_{0.05}(Im)_2(ImH)_2]$ at T = 300 K.

spezies	g	B_2^0 (MHz)	B_2^2 (MHz)	B_4^0 (MHz)	B_4^2 (MHz)	B_4^4 (MHz)	sample
A	1.9936 ±0.0010	310 ±15	80 ±20	- 0.55 ±0.25	0.80 ±0.12	2.40 ±1.00	$^{3}_{\infty}[Sr_{1-x}Eu_x(Im)_2]$ x = 0.01; 0.05
B	1.9940 ±0.0010	480 ±20	90 ±30	- 0.5 ±0.20	not determined	32 ±10	$^{3}_{\infty}[Sr_{1-x}Eu_x(Im)_2]$ x = 0.05
C	1.9940 ±0.0010	410 ±20	60 ±30	-0.70 ±0.25	0.40 ±0.20	3.40 ±1.00	$^{3}_{\infty}[Sr_{0.95}Eu_{0.05}(Im)_2(ImH)_2]$

Tab. 3: Temperature dependence of selected zfs parameters of the Eu^{II} species A in $^{3}_{\infty}[Sr_{0.99}Eu_{0.01}(Im)_2]$.

T (K)	B_2^0 (MHz)	B_2^2 (MHz)	B_4^2 (MHz)
300	310	80	0.80
250	305	86	0.72
100	300	90	0.63
150	295	92	0.58
100	290	94	0.50
50	285	96	0.46
5	280	96	0.46

Tab. 4: Temperature dependence of selected zfs parameters of the Eu^{II} species B in $^{3}_{\infty}[Sr_{0.95}Eu_{0.05}(Im)_2]$.

T (K)	B_2^0 (MHz)	B_2^2 (MHz)	B_4^4 (MHz)
300	480	90	32
15	390	70	25

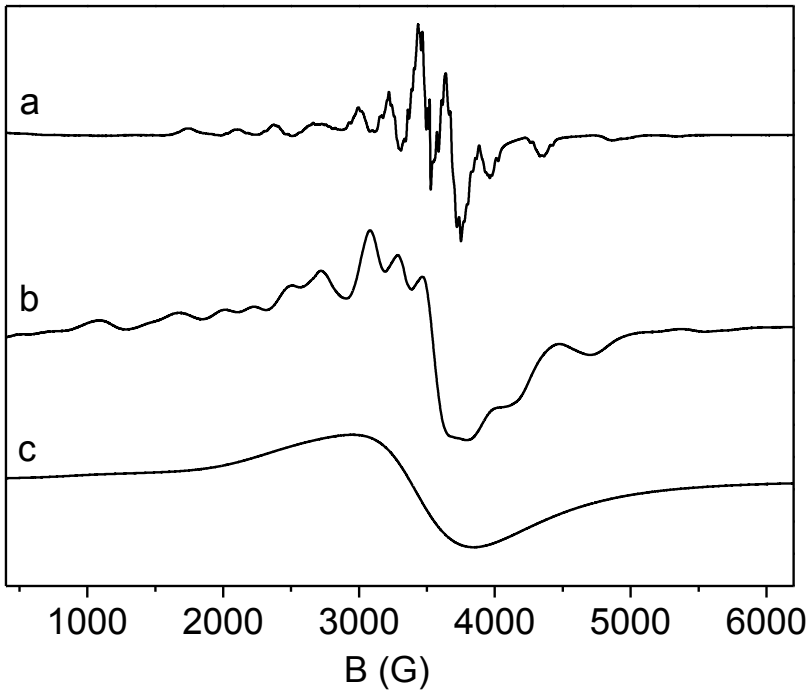

Fig. S13: Eu^{II} X-band EPR spectra of $^{3}_{\infty}[Sr_{1-x}Eu_x(Im)_2]$ with (a) x = 0.01, (b) x = 0.05 and (c) x = 1 recorded at *T* = 300 K.

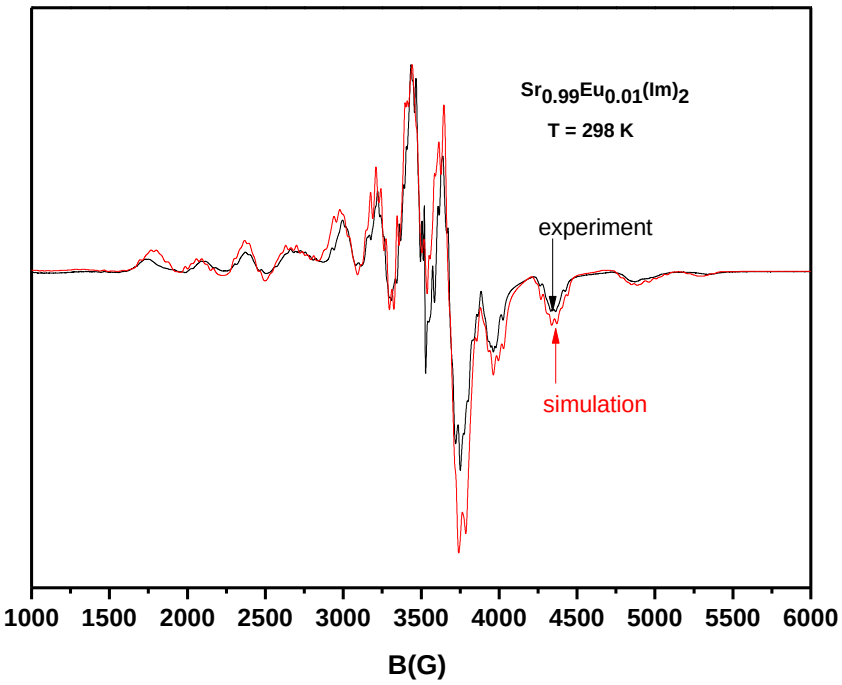

Fig. S14: Experimental and simulated X-band EPR spectra of Eu^{II} species A in $^{3}_{\infty}[Sr_{0.99}Eu_{0.01}(Im)_2]$.

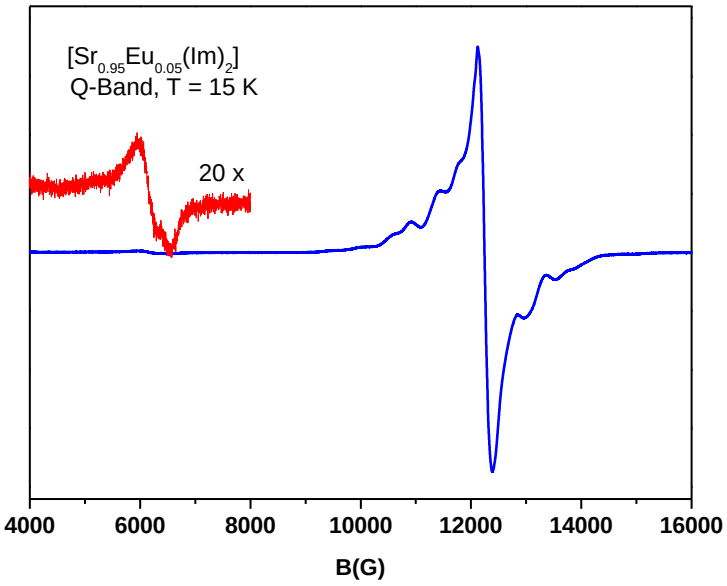

Fig. S15: Experimental Q-band EPR spectrum of $^{3}{}_{\infty}[Sr_{0.95}Eu_{0.05}(Im)_2]$ at T = 15 K showing a forbidden $\Delta M_S = \pm 2$ transition at half field (6000 G) which is typical for high spin systems.

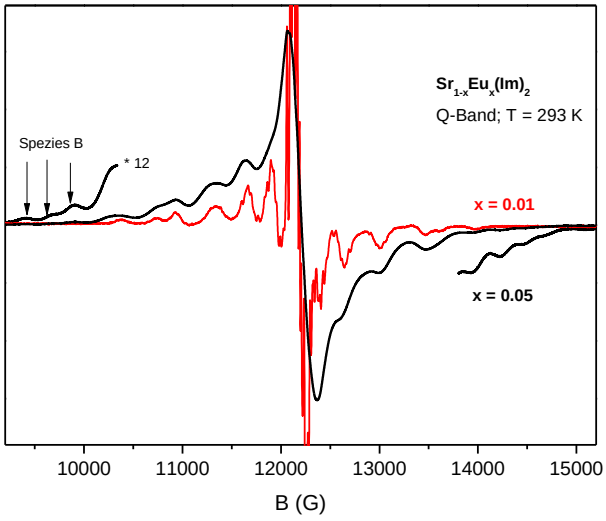

Fig. S16: Comparison of Q-band EPR spectra of $^{3}{}_{\infty}[Sr_{1-x}Eu_x(Im)_2]$ x = 0.01; 0.05 at T = 293 K showing the additional spectrum of Eu^{II} species B for the sample with x = 0.05.

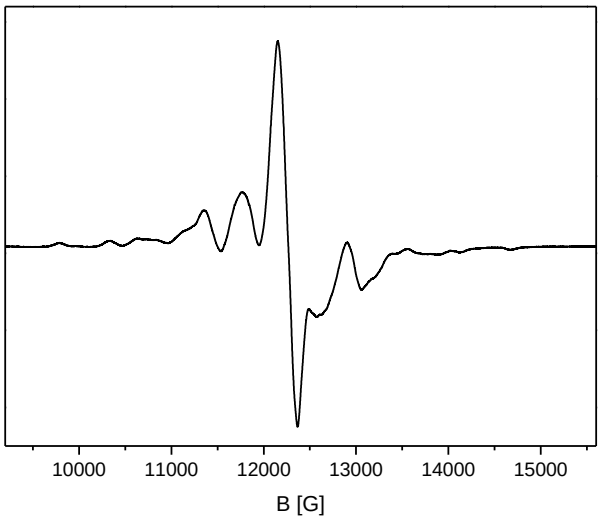

Fig. S17: Q-band EPR spectrum of Eu^{II} species C in $^{3}_{\infty}[Sr_{0.95}Eu_{0.05}(Im)_2(ImH)_2]$ at T = 293 K.

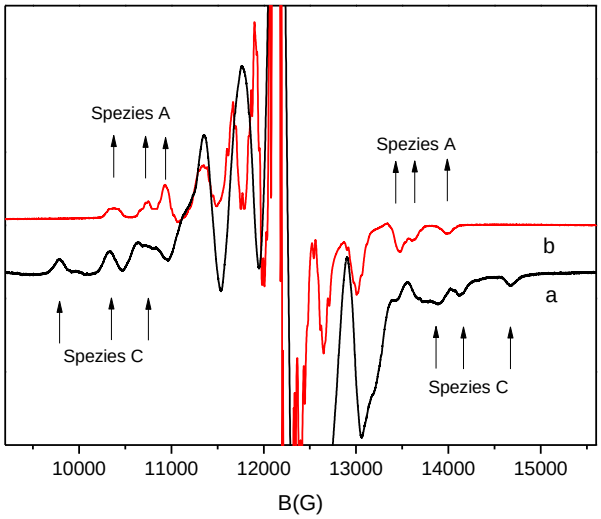

Fig. S18: Comparison of Q-band EPR spectra of (a) $^{3}_{\infty}[Sr_{0.95}Eu_{0.05}(Im)_2(ImH)_2]$ and (b) $^{3}_{\infty}[Sr_{0.99}Eu_{0.01}(Im)_2]$ at T = 295 K showing the two Eu^{II} species A and C.

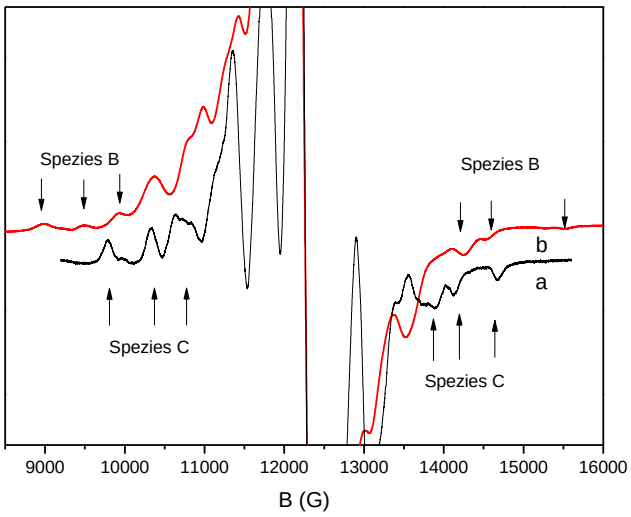

Fig. S19: Comparison of Q-band EPR spectra of (a) $^{3}_{\infty}[Sr_{0.95}Eu_{0.05}(Im)_2(ImH)_2]$ and (b) $^{3}_{\infty}[Sr_{0.95}Eu_{0.05}(Im)_2]$ at T = 295 K showing the two Eu^{II} species B and C. The more intense peaks in the spectrum of $^{3}_{\infty}[Sr_{0.95}Eu_{0.05}(Im)_2]$ are due to species A.

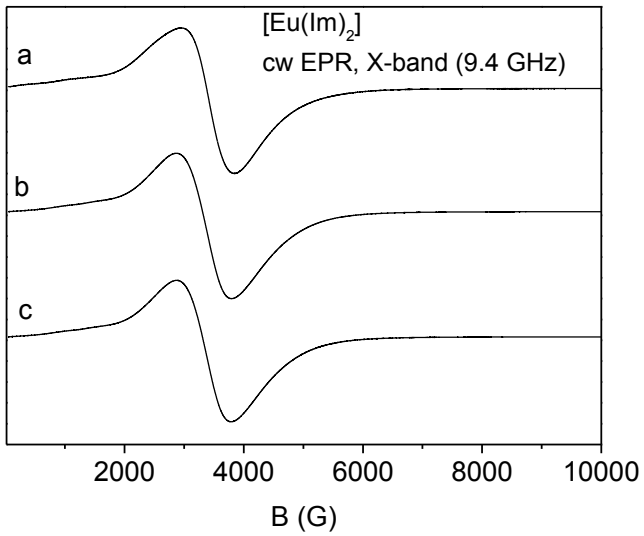

Fig. S20: X-band Eu^{II} EPR spectra of $^{3}_{\infty}[Eu(Im)_2]$ at (a) T = 295 K, (b) T = 8 K in the dark, and (c) T = 8 K under illumination with the full spectrum of a mercury arc lamp.

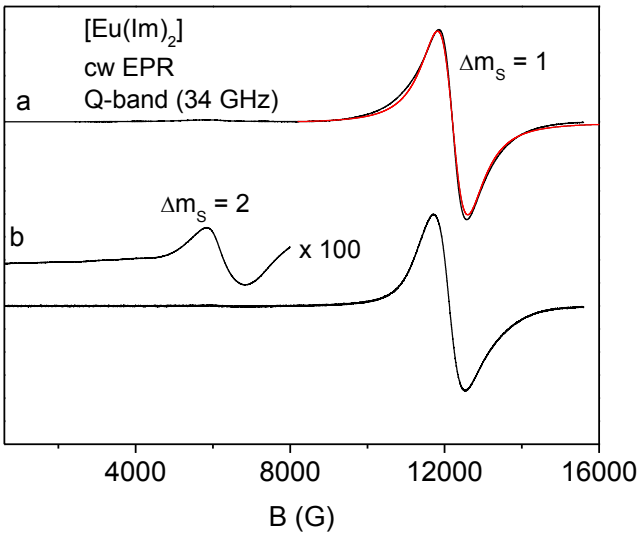

Fig. S21: Q-band Eu^{II} EPR spectra of $^{3}{}_{\infty}[Eu(Im)_2]$ at (a) T = 295 K and (b) T = 8 K. The red line illustrates the fit of the resonance line belonging to the $\Delta M_S = \pm 1$ transitions with an Lorentzian line (parameters: g = 1.9924, ΔB_{pp} = 774 G).

References

[1] Abragam, A.; Bleaney, B.; *Electron Paramagnetic Resonance of Transition Metal Ions*, 1970, Claendon Press, Oxford.
[2] Stoll, S.; Schweiger, A.; *J. Magn. Reson.* **2006**, *178*, 42.
[3] Van Vleck, J.H.; *Phys. Rev*. **1948**, *74*, 1168.
[4] Zurawski, A et. al., *Chem. Comm*. **2011**, *47*,496.
[5] Bljumenfeld, L. A:; Wojewodski, W. W.; Semjonow, A. G.; *Die Anwendung der Paramagnetischen Elektronenresonanz in der Chemie*, 1966, Akademische Verlagsgesellschaft Geest & Portig K.-G., Leipzig.
[6] Anderson, P. W.; Weiss, R. R.; *Rev. Mod. Phys.* **1953**, *25*, 269.